Untethered bistable origami crawler for confined applications

*Catherine Jiayi Cai 1,2, Hui Huang 2, and Hongliang Ren 1,3**

1. Department of Biomedical Engineering, National University of Singapore, Singapore 117575, Singapore;

2. Singapore Institute of Manufacturing Technology, Singapore 138634, Singapore

3. Department of Electronic Engineering, Faculty of Engineering, The Chinese University of Hong Kong, China

* Corresponding to hlren@ieee.org

This PDF file includes:

Supplementary Text

Fig. S1 to Fig. S14

Table. S1 to S3

Legends for Supplementary Movies S1 to S5

SI References

Other Supplementary Material for this manuscript includes the following:

Supplementary Movies S1 to S5

Supplementary Text

1. Crease pattern parameters in the design of the Bistable V-fold unit

Choice of $\boldsymbol{\theta_V}$. We consider the V-fold cylindrical origami that was made up of iterative layers each consisting of mirroring V-folds that globally fold to form a cylindrical span. According to [1], the V-folds are characterized by their distinctive 'V' shape, in which three mountain folds and one valley fold (or one mountain fold and three valley folds) meet at a node. The individual V-folds achieve targeted folding angles by kinematically coupling with other folding angles [2]. Depending on the angle between the strokes of each V (V-fold angle, θ_V), we can open or close the span [1]. Fig. S1 (a) shows the generic crease pattern of a four-sided V-fold cylindrical bellows with a θ_V of 90° (also commonly known as the accordion bellow), and the folded counterpart generated using an online origami simulator [3]. Similar to the Kresling, V-fold cylinders are flat-foldable but not rigid-foldable. This can be attributed to Conelly's bellows theorem [4], [5]. Unlike the Kresling however, the cylindrical V-fold pattern is able to generate purely translational motion.

The folding angle of the crease pattern can greatly influence the geometry of the folded origami cylinder. A larger folding angle ($\theta_V \geq 90°$) created a smaller closing angle ($\phi_V \leq 90°$) to allow for a greater span, resulting in a more rounded and cylindrical tubular structure with polygonal faces. In contrast, a smaller folding angle ($\theta_V \leq 90°$)) created a larger closing angle ($\phi_V \geq 90°$), resulting in a more angled and compact box-like structure. Fig. S1 (b) shows the crease patterns of the V-fold origami for θ_V = 60°, 90° and 120°, along with the simulated folded counterparts. Due to space constraints in confined regions, we preferred larger closing angles in the design of the origami crawler due to its compactness. However, at larger θ_V, the folding of the origami pattern risked collision within each layer. To avoid this, we modified the crease pattern by halving the crease pattern and included straight folds that could be folded in and glued together to create an enclosed structure (Fig. S1 (c)).

Choice of $\boldsymbol{\theta_H}$. As the V-fold pattern was non-rigid foldable like the Kresling, V-fold cylinders were rarely fully extended to avoid over-straining the vertices which could cause the creases to invert, resulting in undesirable buckling and deformation [6]. As such, V-fold cylinders were often designed to be unimodally stable and inherently compliant. Silverberg et al [7] noted that for real physical materials that could bend, there existed a hierarchy of degree of freedom (DoF) that each have their own associated energy scale. Elaborating on this, they demonstrated how non-rigid foldable origami exhibits hidden bending DoFs that were separated from the crease DoF by an energy gap, giving rise to a critical bifurcation between mono-stability and bistability that was geometrically driven.

Upon unfolding a module of the modified V-fold origami pattern, we observed that beyond a certain unfolding angle, the facets began to bend during the unfolding process, eventually causing the valley crease to invert and access a different configuration (Fig. S2 (a)). In addition, the structure was able to hold this configuration even in the absence of external force, indicating that the origami module had reconfigured into a different stable state. Silverberg et al [96] referred to this phenomenon as an energy-scale dependent DoF that resulted from the geometry of creased sheets in constraint-based compliant materials.

Similar to Melancon et al [8], we further modified the crease pattern of the V-fold origami by placing mountain creases of an angle (θ_H) where the observed outward bending of the facets occurred to invert the valley crease, creating a degree-four vertex (Fig. 1 (a)). Under sufficient external forces, the creases around these vertices were observed to inflect locally, causing the V-fold origami to deploy into the other configuration. The deployed configurations of the folded prototypes with defined and undefined θ_H are shown in Fig. S2 (b)

Choice of $\boldsymbol{\theta_B}$. Upon deployment of the bistable V-fold module, it adopted a rigid curved configuration with a tunable bending radius (ϕ_B) governed by the ratio of the of the height (b) and half-length (a) of the triangulated V-fold in each unit of the bistable V-origami crease pattern (Fig 3.16 (a)). From geometry, the angle θ_B was calculated to be:

$$\theta_B = 2 * \tan^{-1}\left(\frac{a}{b}\right) \tag{1}$$

We further measured the bending radius ϕ_B of the folded deployed bistable V-fold origami module corresponding to their respective θ_B and best-fitted the results in Origin (Fig. S3 (c)). We observed that the relationship between the two could be approximated as such:

$$\phi_B = 1.22 * \theta_B - 12.2 \tag{2}$$

When combinations of individual bistable V-fold modules were deployed in an aggregated bistable V-fold origami, the resulting structure was compliant around a bending axis up to a specific angle, at which it was unable to bend further due to the inherent structure (Fig S3 (b)). The minimum bending angle ($Total\phi_B$) that the structure can achieve was approximated to be the sum of the bending radius ϕ_B of the individual deployed V-fold origami modules.

In this work, we chose $\theta_B = 45°$ as an arbitrary value. Depending on the desired bending radius of the application, θ_B can be tuned accordingly.

2. Fabrication of the bistable V-fold mechanism

V-fold Origami. The crease pattern of the origami mechanism was drawn in Inkscape with a line thickness of 0.1 mm, and the crease lines as a series of small holes in a straight line. We used $50\,\mu\text{m}$ think Polyethylene Terephthalate (PET) sheets (purchased from Jubang plastic material, Inc.) for the folding of the origami mechanisms in this work. The material then defined in the lasercut software (xTool Creative Space) was "Brown Kraft Paper" of 0.2 mm thickness (Fig. S4 (a)). The laser parameters were set to “cut” with a flat laser, with the power and speed set at 40% and 15 respectively for a total of 1 pass (Fig. S4 (b)). Three units of bistable origami V-fold is then folded and the glue tabs are adhered together using silicone adhesive (Cutorin 4672-B food grade silicone). To maximize the translation of the torque that the IPMs experience under the influence of the EPM to the folding and unfolding of the central crease, the side units housing the IPMs are clamped to the central unit using silicone adhesive to remove the folding DoFs of the side units.

Internal Permanent Magnets (IPMs). To a three-unit bistable origami V-fold mechanism, we tucked and attached an N35 permanent disc magnet (5 mm diameter, 1 mm thickness, purchased from Titan™ Magnetics) into each end of the folded mechanism (in each end unit of the crease pattern) such that their magnetic moments mirrored each other (Fig. S4 (b)). The disc magnets were chosen because their flatness enabled them to integrate well with the flat foldable nature of the V-fold origami. While the diameter of the IPM was arbitrary, we chose the maximum size that could fit into the origami as a larger magnet was usually associated with greater magnetic flux and hence could be actuated using weaker magnetic fields [9]. Food grade silicone adhesive was used to adhere the IPMs to the V-fold mechanism.

3. <u>Magnetic Actuation of the bistable V-fold mechanism</u>

External Permanent Magnet (EPM). We used an N52 neodymium-iron-boron (NdFeB) alloy cube magnet (side 25 mm) from Titan™ Magnetics as the EPM. Similar to the IPMs, the size and shape of the EPM used can be arbitrary, as long as it was able to generate sufficiently strong enough magnetic fields for the intended purpose.

Principles of magnetic actuation. Fig. S5 (a) shows a representation of a magnetic dipole (of magnetic moment $\mathbf{m}$) generating magnetic field lines that are radially symmetrical about its magnetization direction According to [10], the magnetic field $\mathbf{B}$ generated tangent to the magnetic field lines by a magnetic dipole (located at $\mathbf{P_m}$) on a region of interest (located at $\mathbf{P_b}$) can be approximated by the dipole model as:

$$\mathbf{B}\{\mathbf{r},\mathbf{m}\} = \frac{\mu_0}{4\pi|\mathbf{r}|^3}(3\hat{\mathbf{r}}\hat{\mathbf{r}}^{\mathrm{T}} - \mathbf{I})\mathbf{m} \tag{3}$$

where $\mu_0 = 4\pi \times 10^{-7}\ \mathrm{T}\cdot\mathrm{m}\cdot\mathrm{A}^{-1}$ is the permeability of free space, $\mathbf{r} = \mathbf{P_b} - \mathbf{P_m}$, and $\mathbf{I}$ is the identity matrix.

Upon interaction between the permanent magnets, the magnetic field from the EPM generates forces and torques that, if strong enough to overcome the inherent folding stiffness of the creases, can induce unfolding and folding and consequently deployment and Undeployment respectively of the bistable origami mechanism respectively. The resulting force (*f*) and torque (τ) imposed on an IPM (and consequently on the origami crawler backbone) can be calculated using the following equations:

$$f_i = \nabla(\mathbf{m_i}\cdot\mathbf{B_i}) \tag{4}$$

$$\tau_i = \mathbf{m_i}\times\mathbf{B_i} \tag{5}$$

where $f_i, \tau_i \in \mathbb{R}^3$, (*i* = 1,2,3), $\mathbf{m_i}$ is the magnetic dipole of the IPM located at position $\mathbf{P_i}$, and $\mathbf{B_i}$ is the magnetic field generated on the IPM at location $\mathbf{P_i}$ by the other IPMs and EPM. In the absence of a sufficiently strong magnetic field generated on the IPMs, the innate elasticity of crawler backbone and gravity will restore it to its original shape.

Expanding on equations (4) and (5), the forces f and torques τ exerted on the IPMs due to the magnetic field generated by the EPM can be modelled as:

$$
\mathrm{f_{IPM}} = \frac{3\mu_0}{4\pi|\mathbf{r_\alpha}|^4}[(\widehat{\mathbf{r_\alpha}}^{\mathrm{T}}\mathbf{m_{IPM}})\mathbf{m_{EPM}} + (\widehat{\mathbf{r_\alpha}}^{\mathrm{T}}\mathbf{m_{EPM}})\mathbf{m_{IPM}} + \left(\mathbf{m_{EPM}}^{\mathrm{T}}\mathbf{m_{IPM}} - \mathbf{5}(\widehat{\mathbf{r_\alpha}}^{\mathrm{T}}\mathbf{m_{EPM}})(\widehat{\mathbf{r_\alpha}}^{\mathrm{T}}\mathbf{m_{IPM}})\right)\mathbf{r_\alpha}] \tag{6}
$$

$$
\tau_{\mathrm{IPM}} = \mathbf{S}\{\mathbf{m_{IPM}}\}\left[\frac{\mu_0}{4\pi|\mathbf{r_\alpha}|^3}(\mathbf{3}\widehat{\mathbf{r_\alpha}}\widehat{\mathbf{r_\alpha}}^{\mathrm{T}} - \mathbf{I})\right]\mathbf{m_{EPM}} \tag{7}
$$

Where $\mathrm{r_a}$ is the distance between the EPM and the IPM, $\mathbf{m_{EPM}}$ is the magnetic moment of the EPM, and $\mathbf{S}\{\mathbf{m_{IPM}}\}$ is the skew-symmetric matrix packing of a vector used in the cross-product operation.

It is worth mentioning that given the size of the origami module, the IPMs were fixed and positioned such that the magnetic field generated between the two IPMs were not negligible. In particular, because the magnetic moment of the IPMs mirrored each other, the IPMs were constantly repelling each other and both IPMs experience an “outwards” rotational moment. In the absence of an externally generated magnetic field, the forces and torques acting on an IPM (IPMa) by the other (IPMb) can be modelled as:

$$
f_{IPMa} = \frac{3\mu_0}{4\pi|\mathbf{r_\beta}|^4}[(\widehat{\mathbf{r_\beta}}^{\mathrm{T}}\mathbf{m_{IPMa}})\mathbf{m_{IPMb}} + (\widehat{\mathbf{r_\beta}}^{\mathrm{T}}\mathbf{m_{IPMb}})\mathbf{m_{IPMa}} + \left(\mathbf{m_{IPMb}}^{\mathrm{T}}\mathbf{m_{IPMa}} - \mathbf{5}(\widehat{\mathbf{r_\beta}}^{\mathrm{T}}\mathbf{m_{IPMb}})(\widehat{\mathbf{r_\beta}}^{\mathrm{T}}\mathbf{m_{IPMa}})\right)\mathbf{r_\beta}] \tag{8}
$$

$$
\tau_{IPMa} = \mathbf{S}\{\mathbf{m_{IPMa}}\}\left[\frac{\mu_0}{4\pi|\mathbf{r_\beta}|^3}(\mathbf{3}\widehat{\mathbf{r_\beta}}\widehat{\mathbf{r_\beta}}^{\mathrm{T}} - \mathbf{I})\right]\mathbf{m_{IPMb}} \tag{9}
$$

Where r_β is the distance between IPMa and IPMb, $\mathbf{m_{IPMa}}$ and $\mathbf{m_{IPMb}}$ are the magnetic moments of IPMa and IPMb respectively, and $\mathbf{S}\{\mathbf{m_{IPMb}}\}$ is the skew-symmetric matrix packing of a vector used in the cross-product operation.

When the EPM was brought sufficiently close, the combination of the forces and torques acting on the IPM could be calculated as the summation of equations (6) and (8) for the total force, and equations (7) and (9) for the total torque.

Characterisation of the EPM. We measured the magnetic field generated by the north and south pole of the N52 EPM ($|\mathbf{B}|_{\mathrm{EPM}}$) at different distances |r| from its center using a magnetometer (TD8620, Tunkia Co., Ltd) as shown in Fig S5 (b). A linear motor rail (speed of 2000 pulse/rev) was used to vary the distance of the EPM from the sensor probe of the magnetometer. The initial and final position of the EPM relative to the sensor probe was measured, and the trajectory of the EPM and respective reading sensor reading of the magnetometer was videoed by an Iphone X at 30 FPS. The open-source Physlets Tracker video analysis and modelling tool (Copyright (c) 2019 Douglas Brown) [11] was used to track the relative trajectory of the EPM respective to the magnetometer’s reading at each time step of 0.1 seconds. The absolute distance travelled by the center EPM in each time step was then calculated. We then best-fitted the results in Origin to obtain an estimation of the relationship between the magnetic field strength and the distance from the center of the magnet. Even though equation (3) implied an inverse cubic relationship between the magnetic field $\mathbf{B}$ generated and the distance |r|, we found that an exponential decay was able to better able to fit the data within the measured range (Fig. S5 (c)-(d)).

Magnetic Actuation of the bistable V-fold. To estimate the strength of the magnetic field needed to deploy and un-deploy the bistable V-fold module, we anchored the origami mechanism onto a 3D printed base (PLA) and used a linear motor rail to vary the distance of the EPM from the center of the origami module (Fig S6). For analysis purposes, we set the center of the base of the origami as the origin and vary the y-position of the EPM with its x- and z- position fixed at zero relative to the origin (Fig 1 (c)-(d)). A mirror was used to minimize parallax error that may arise during recording. We then tracked the distance of the EPM relative from the origin (and by extension the origami mechanism), and the corresponding displacement d of the origami mechanism as a result of the folding and unfolding of the middle crease between the two degree-four vertices. We then calculated the corresponding estimated magnetic field of the EPM ($|\mathbf{B}|_{\mathrm{EPM}}$) from the best-fit equations obtained in Fig S6 (c)-(d). In total, three bistable V-fold samples were used and the distance of the EPM required to deploy and undeploy each sample were measured for 3 cycles (Fig S7). The distance from the center of the EPM to the bistable V-fold origami and the respective estimated magnetic field required to deploy and undeploy the samples were then averaged and the standard deviation (STDEV) was obtained from excel (Table. S1 and. S2).

4. Fabrication of the bistable origami crawler

Side Segments. The side segments of the origami crawler was fabricated from 50 μm thick PET sheet via the same laser cutting parameters as the bistable V-fold mechanism. For simplicity, we chose the same set of parameters for the side segments as that of the bistable V-fold (i.e. $\theta_V = \theta_H = 120°$, and $\theta_B = 45°$). The number of units in the left and right segments were chosen to optimize the deformation of the crawler to achieve the desired shapes. When the number of units was too little, the origami crawler was not able to undergo sufficient deformation to achieve the required curvature without deploying. On the other hand, if the number of layers was too great, the origami crawler would be too underactuated and difficult to control.

Assembly of the origami crawler. Food-grade silicone adhesive (Cutorin 4672-B food grade silicone) was used to attach the IPMs and the segments together. Similar to the bistable origami V-fold mechanism, an N35 permanent disc magnet (5 mm diameter, 1 mm thickness, purchased from Titan™ Magnetics) was adhered to one external ends of the origami crawler in the desired orientation.

5. Magnetic actuation of the bistable origami crawler

Magnetic Actuation of the bistable V-fold. Besides the two IPMs located in the central segment, the other IPMs were positioned sufficiently far apart so that the effects they had on each other were negligible enough to be overcome by the inherent folding stiffness of the origami segments. To estimate the strength of the magnetic field needed to shape-morph the origami crawler and deploy and un-deploy the central bistable V-fold mechanism, we used a linear motor rail to vary the distance of the EPM from the center of the origami crawler (Fig S8). The origami crawler was actuated on Ecoflex 00-10 to reduce potential slippage that may arise from being actuated on a smoother surface with less friction. For analysis purposes, we set the center of the base of the origami crawler in its resting configuration as the origin and vary the y-position of the EPM with its x- and z- position fixed at zero relative to the origin. We then tracked the distance of the EPM relative from the origin (and by extension the origami crawler), and the corresponding displacement d of the left, center and right segments of the origami crawler. We then calculated the corresponding estimated magnetic field of the EPM ($|\mathbf{B}|_{\mathrm{EPM}}$) from the best-fit equations obtained in Fig S6 (c)-(d). The folding angle of the central unit of each segment (ϕ_{UL}, ϕ_{UC} and ϕ_{UR}) can be calculated via trigonometry using the cosine law as (Fig. S9):

$$\phi_U = \cos^{-1}(1 - \frac{d^2}{2a^2}) \tag{10}$$

Directional locomotion. We used the same setup where a linear motor rail was used to vary the distance of the EPM from the base of the origami crawler (Fig. S10). The origami crawler was actuated on Ecoflex 00-10 to reduce potential slippage that may arise from being actuated on a smoother surface with less friction. For analysis purposes, we set the center of the base of the origami crawler in its resting configuration as the origin and vary the y-position of the EPM with its z- position fixed at zero relative to the origin. However, we fixed the x-position of the EPM at varying values relative to the central segment. We then tracked the y-position of the EPM relative to the origin (and by extension the origami crawler), and the corresponding x-position of the central unit of each segment was used to represent the displacement of the origami crawler. As per our nomenclature, the right segment indicated the front segment and a positive change in x position indicated forward displacement of the origami crawler.

The x-position of the north pole of the EPM relative to the center of the origami spring determines whether the origami spring was able to achieve directional locomotion. As observed in Fig. S11 (a), positioning the north pole of the EPM ahead of the center of the origami spring caused an initial forward displacement due to the anchoring of the front segment, pulling the rear end forward (①-②). When the EPM was not sufficiently ahead of the center of the origami spring (6.5 mm in this case), the origami spring would slide backwards after the initial forward displacement upon moving the EPM away, resulting in little to no net displacement (②-④). This was because the magnetic field acting on the front IPM was too strong that even upon moving the EPM away, the front end was still bent and remained more anchored relative to the back end. Hence, the back end of the origami spring slid backwards instead, resulting in little to no net displacement. However, when the EPM was placed too far ahead of the center of the origami spring (18 mm in this case) as in Fig. S11 (b), the origami spring would undergo forward slippage during the anchoring phase of the front end (②-③), which was undesirable.

Crawling speed of the origami crawler. We manually actuated the origami crawler on Ecoflex 00-10 at different frequencies for ~ 20 s. We tracked the position of the center of the crawler over time using the Physlets tracker, which was used to reflect the distance the crawler travelled (Fig. S12 (a)). We chose to use Ecoflex as the travelling material as it was commonly used as tissue phantoms and models in literature as they possessed similar stiffness to that of biological tissues [12]–[14][15]–[17]. We actuated at origami crawler at three different frequencies for three cycles each:

1.0 Hz, 1.25 Hz and 1.5 Hz. A metronome was used to ensure actuation of the origami crawler at a consistent frequency (60 bpm = 1.0 Hz, 75 bpm = 1.25 Hz, 90 bpm = 1.5 Hz). The average displacement and standard deviation travelled by the origami crawler was then taken by averaging the displacement values at each time stamp was obtained from excel. From Fig. S12 (d), we observed that the first cycle (C1) of the actuation of the origami crawler at 1.5 Hz is drastically different from the other two cycles and hence excluded from analysis. The travelling speed of the origami crawler is calculated by dividing the total distance travelled by the origami crawler by the total time (~20 s) required for it to cover that distance. The normalized travelling speed (bodylength/s) of the origami crawler is calculated as follows:

$$bodylength/s = \frac{average\ speed}{origami\ crawler\ length} = \frac{average\ speed}{22\ mm} \quad (11)$$

The travelling speed, normalized travelling speed and the respective standard deviation of the origami crawler at each actuation frequency is calculated from excel as shown in Table. S3.

Tilting of the origami crawler. We used the same setup where a linear motor rail was used to vary the distance of the EPM from the base of the origami crawler (Fig. S13). The origami crawler was actuated on Ecoflex 00-10 (~0.5 mm thick) to reduce potential slippage that may arise from being actuated on a smoother surface with less friction. For analysis purposes, we set the center of the base of the origami crawler in its resting configuration as the origin and vary the z-position of the EPM with its x- position fixed at zero relative to the origin. However, we fixed the y-position of the EPM at 25 mm. We then tracked the z-position of the EPM relative to the origin (and by extension the origami crawler), and the corresponding z-position of the origami crawler was used to calculate the tilt angle of the origami crawler.

Navigation of the origami crawler on porcine small intestine. We obtained porcine small intestine from food2homes. A segment of the small intestine was cut open and laid flat to expose the intestinal wall on a 3D printed phantom and adhered using cyanoacrylate to prevent slipping of the small intestine during locomotion of the origami crawler. Most of the mucin was removed from the small intestine surface.

6. Microneedles delivery and insertion

Verification of microneedles insertion. The topology of the microneedles of the CASMA patch as viewed under an optical microscope is shown in Fig. S13 (a), while the topology of an un-punctured Ecoflex (~0.5 mm thick) is shown in Fig. S13 (b). From Fig. S13 (c), visible puncture marks can be observed in the Ecoflex film from the microneedles delivered by the origami crawler. To verify that the puncture marks observed is attributed to the insertion of microneedles, we compared the puncture marks created by the insertion of microneedles by the origami crawler with that made by a commercial spring-loaded applicator (MPatch Mini Applicator, purchased from Micropoints Technology Pte Ltd), which was often used for epidermal microneedle insertion (Fig. S13 (d)). From Fig. S13 (d), we observed an array of puncture holes that verifies that the marks observed on the Ecoflex are due to the insertion of microneedles. The marks observed in both Fig. S13 (c) and (d) bear resemblance, verifying successful puncture of the microneedles into the Ecoflex film by the origami crawler.

It is worth noting that in contrast to the puncture marks made by the commercial spring-loaded applicator, the puncture holes made by the origami spring were less distinct. We attributed this to two reasons. Firstly, while the spring applicator was used to insert the microneedles on a flat uniform surface, the origami spring was used for endoluminal microneedles insertion, which resulted in non-uniform force distribution due to the insertion of microneedles on a curved surface in a tubular environment. Secondly, the amount of force that the origami spring was able to generate from the snap-through bistability was likely to be lesser than that of the spring applicator, and hence the microneedles deployed by the origami spring may not have penetrated the Ecoflex film as deeply as those deployed by the commercial spring applicator. We believe that the force-loading capacity of the origami spring can be further enhanced to improve its microneedles insertion capability. In addition, we believe that coupled with the peristaltic motion in the small intestine, sufficient compressive forces can be exerted by the origami crawler on the intestinal wall for greater contact and penetration insertion of the microneedles for biomedical applications [18].

Supplementary Figures

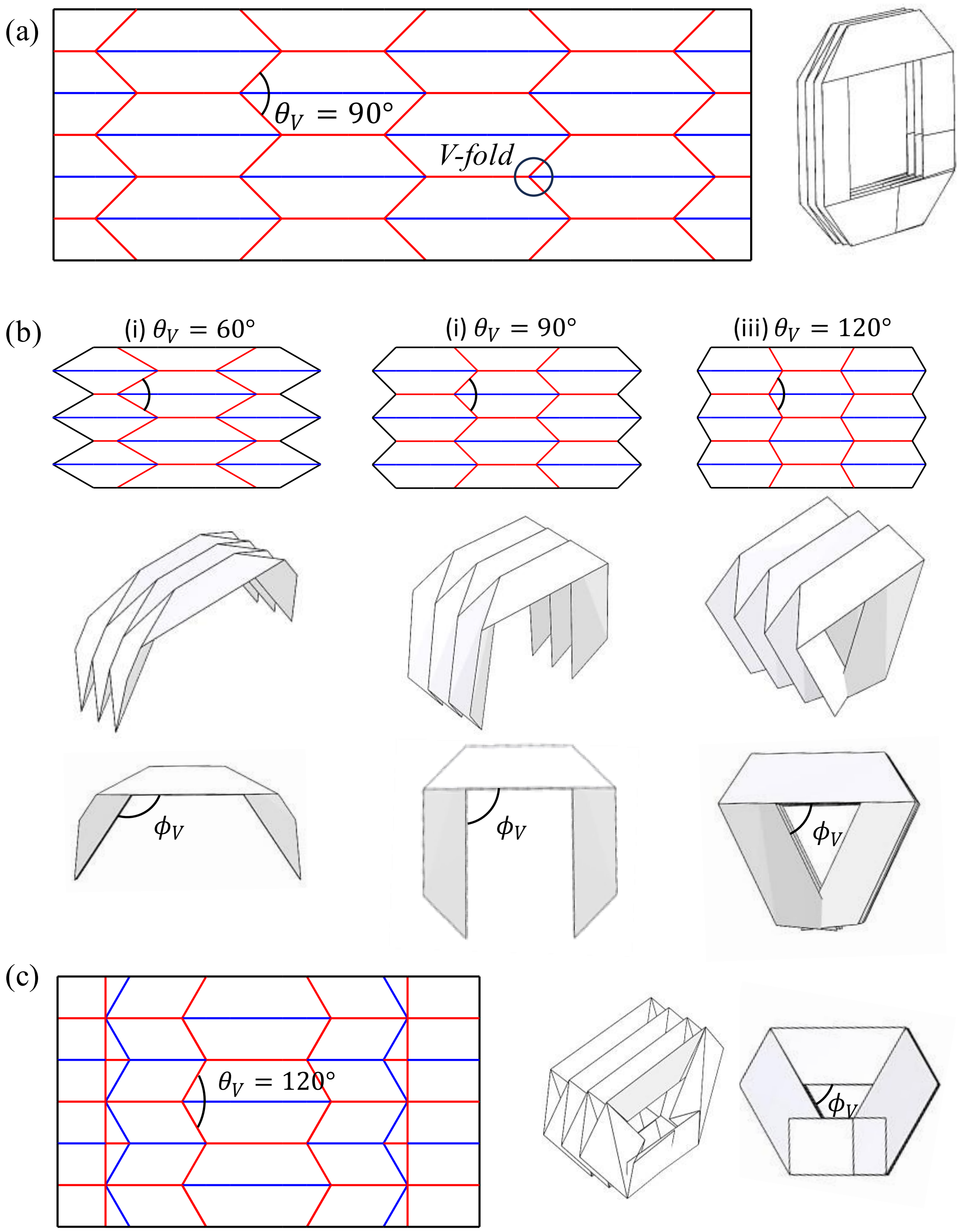

Fig. S 1 Influence of $\boldsymbol{\theta_V}$. (a) Crease pattern and folded counterpart of the accordion bellows consisting of alternating V-folds with an angle $\boldsymbol{\theta_V}$ of 90°. The circle indicates the distinctive V shape where the three mountain folds (red lines) and one valley fold (blue) meet at a node. (b) The crease patterns and the corresponding simulated origami structures when $\boldsymbol{\theta_V}$ = (i) 60°, (ii) 90° and (iii) 120°. A larger folding angle ($\boldsymbol{\theta_V}$) results in a smaller closing angle ($\boldsymbol{\phi_V}$) of the structure and vice-versa. (c) The modified origami crease pattern allowing for folding of V-fold origami with larger folding angles. Here, the folding angle $\boldsymbol{\theta_V}$ = 120°.

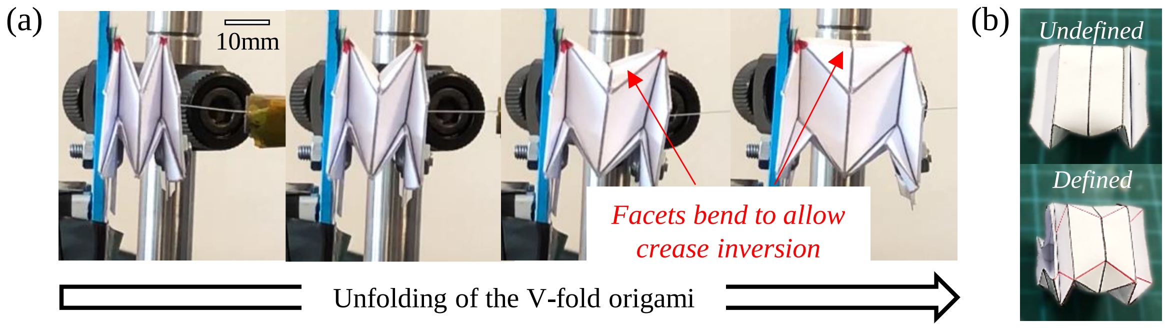

Fig. S 2 Influence of θ_H. (a) Modified bistable V-fold origami demonstrated bistability as a result of energy-scale dependent DoF due to its non-rigid foldable nature. Unfolding the V-fold origami beyond a certain point caused the facets to bend, enabling crease inversion. At this point, the origami entered a different stable configuration. (b) The folded origami with undefined (top) and defined bending creases (bottom).

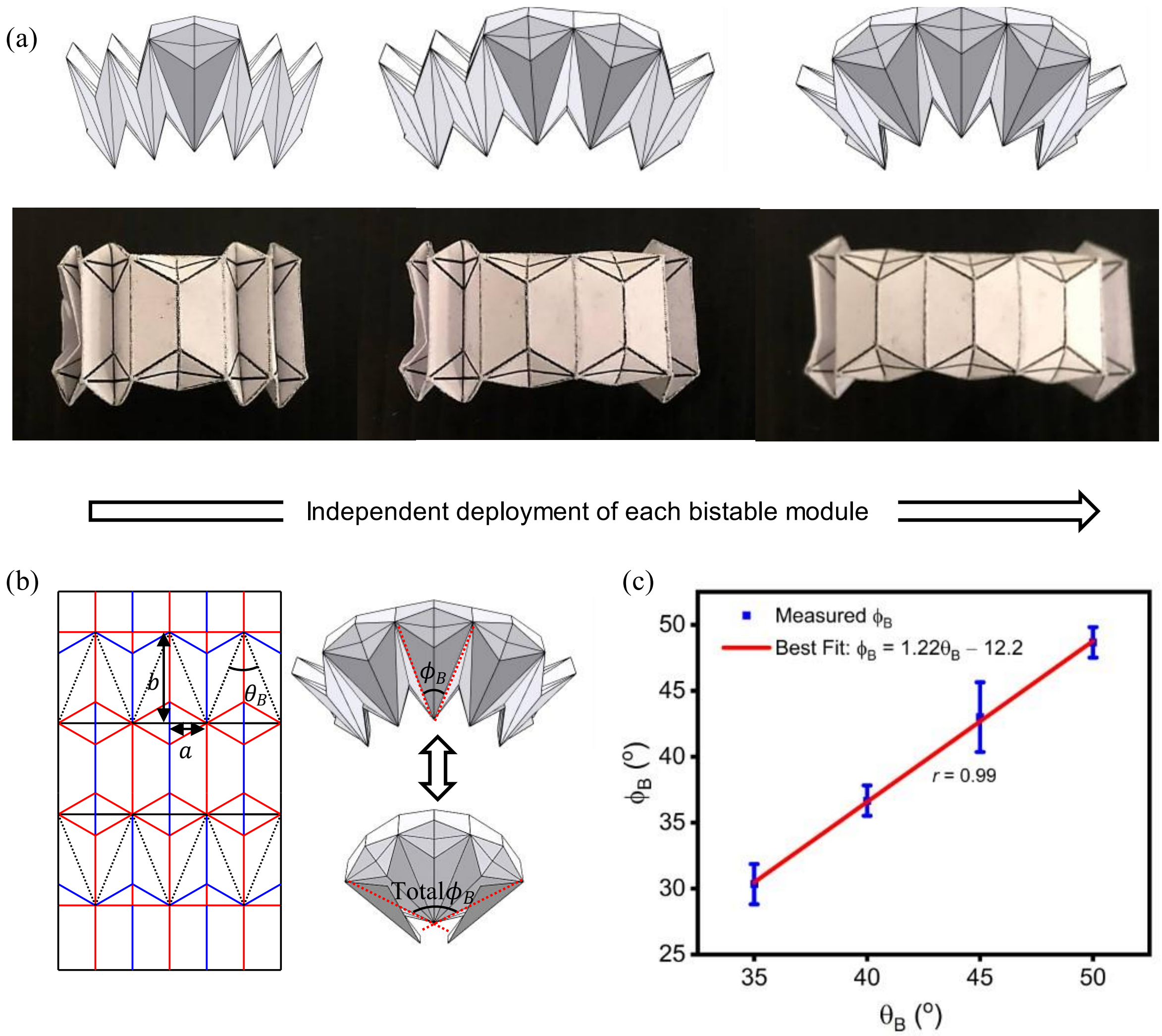

Fig. S 3 Influence of $\boldsymbol{\theta_B}$. (a) Combining several bistable V-fold modules result in an aggregated structure where each module can deploy independently of its neighbouring modules.(b) Bending radius $\boldsymbol{\Phi_B}$ of each deployed V-fold origami module was dependent on the angle $\boldsymbol{\theta_B}$. The minimum bending angle of a fully deployed origami structure consisting of aggregated bistable V-fold origami modules was given as $\boldsymbol{Total\phi_B}$. (c) Linear relationship between $\boldsymbol{\Phi_B}$ and $\boldsymbol{\theta_B}$.

Fig. S 4 Fabrication of miniature bistable V-fold module. (a) Crease pattern of the origami V-fold where the crease lines are drawn as perforated holes. (b) Laser cutting of crease pattern on 50 μm thick PET sheets. (c) Integration of 5 mm x 1 mm discs magnets into the bistable V-fold origami module. IPMs were tucked into the ends of the origami module and oriented in a way that that their magnetic moments mirrored each other.

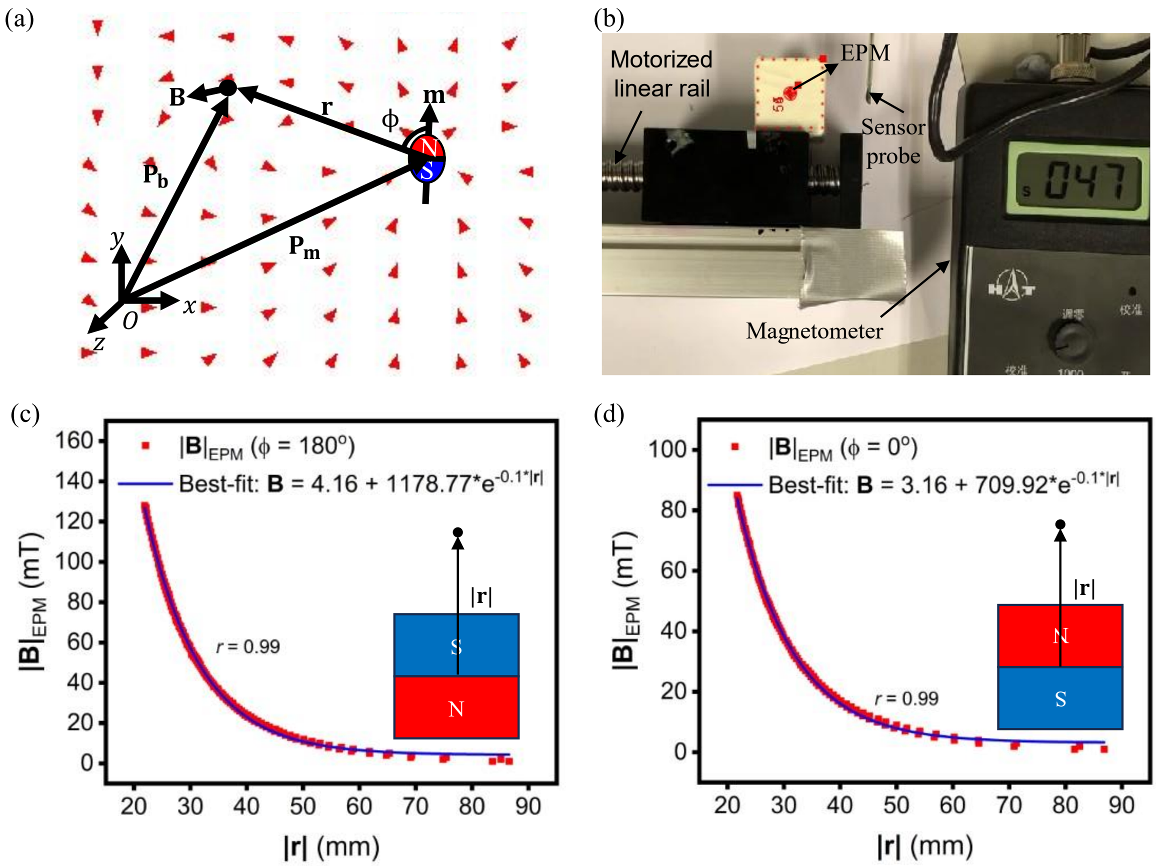

Fig. S 5 Characterisation of EPM. (a) Representation of magnetic field produced by the external permanent magnet as abstracted as a magnetic dipole. (b) Experimental setup where a linearised motor was used to vary the distance between the EPM and the magnetometer. The relative trajectory of the EPM (red circle) and respective magnetic field measurement reflected on the magnetometer was tracked using the open-source Physlets Tracker video analysis and modelling tool (c) Characterisation of the magnitude of the magnetic field generated by the EPM ($|\mathbf{B}|_{\mathbf{EPM}}$) at different distances |r| as measured from its south pole and (d) north pole. The data is best-fitted in origin using an exponential relationship.

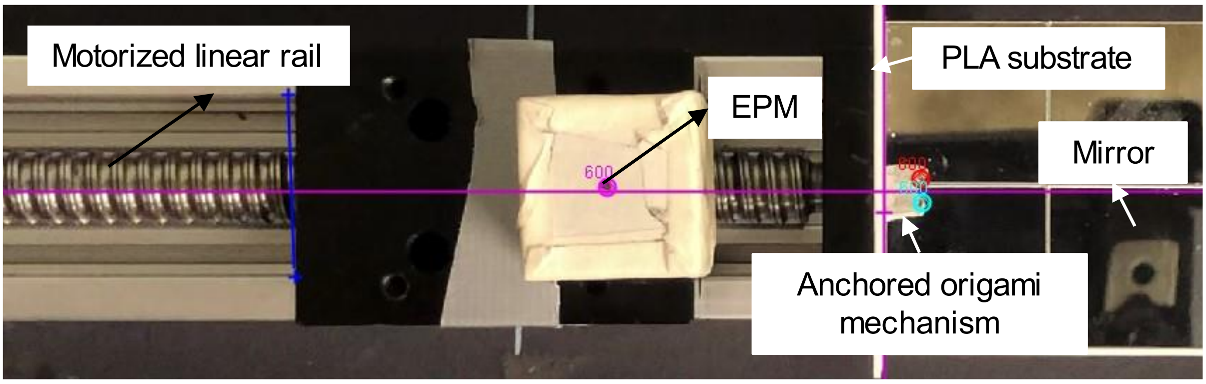

Fig. S 6 Experimental setup for the magnetic Actuation of bistable V-fold origami mechanism. A motorized linear rail was used to vary the y-position of the EPM relative from the origami mechanism to modulate the strength of the induced magnetic field throughout the actuation of the mechanism.

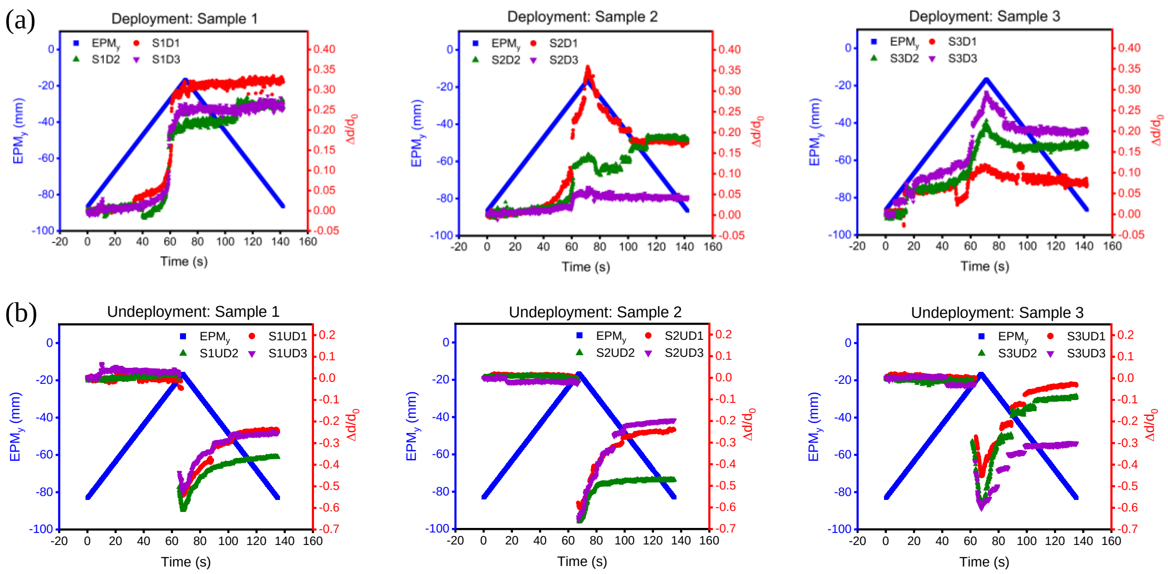

Fig. S 7 Distance from the center of the EPM to the bistable V-fold origami vs deformation of he origami mechanism. (a) Deployment of samples 1 to 3, each for 3 cycles. (b) Undeployment of samples 1 to 3, each for 3 cycles.

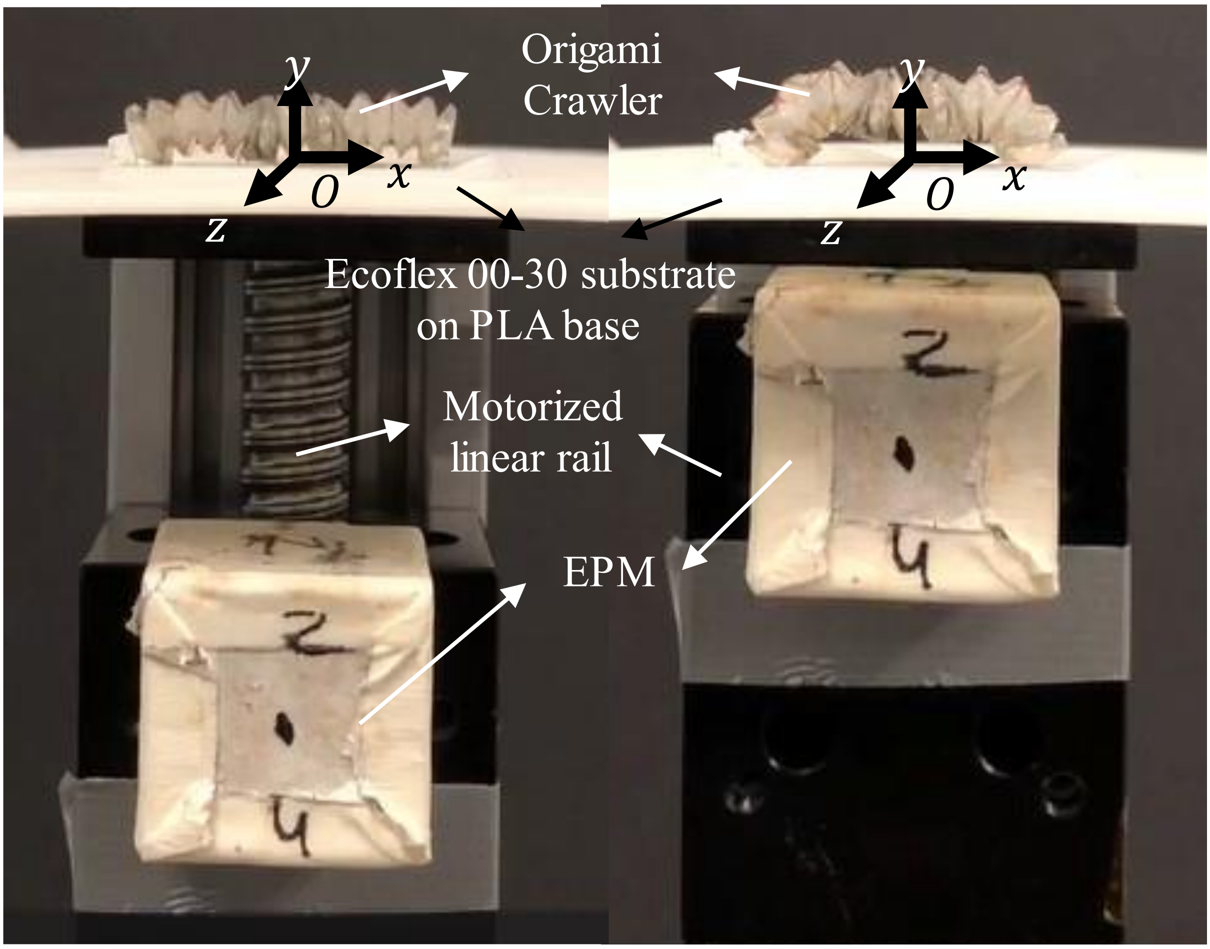

Fig. S 8 Experimental setup for the magnetic actuation of the origami crawler to induce shape-morphing between the deployed and undeployed state. A motorized linear rail was used to vary the y-position of the EPM relative from the origami crawler to modulate the strength of the induced magnetic field throughout the actuation of the mechanism.

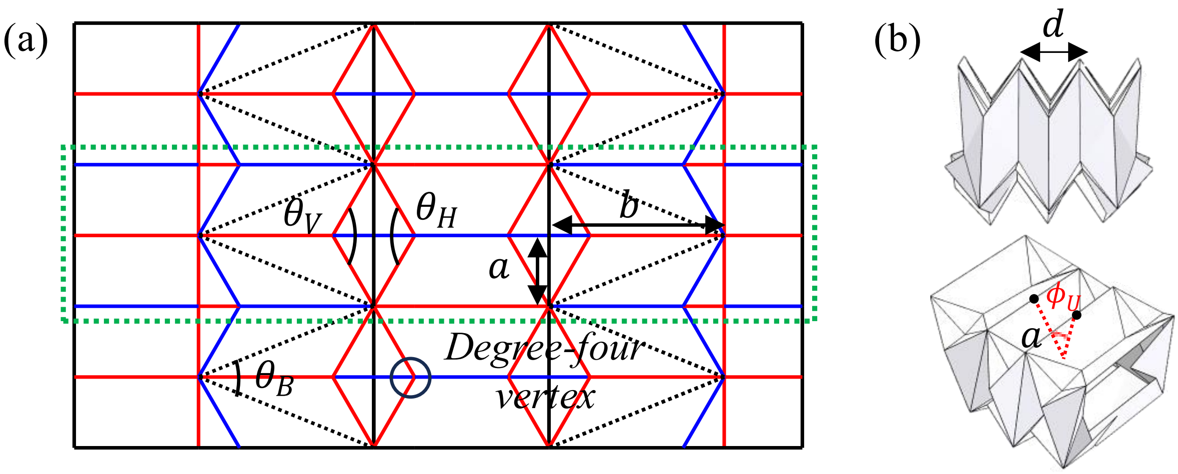

Fig. S 9 Characterisation of Folding angle (ϕ_U). The folding angle of the origami V-fold can be calculated via trigonometry.

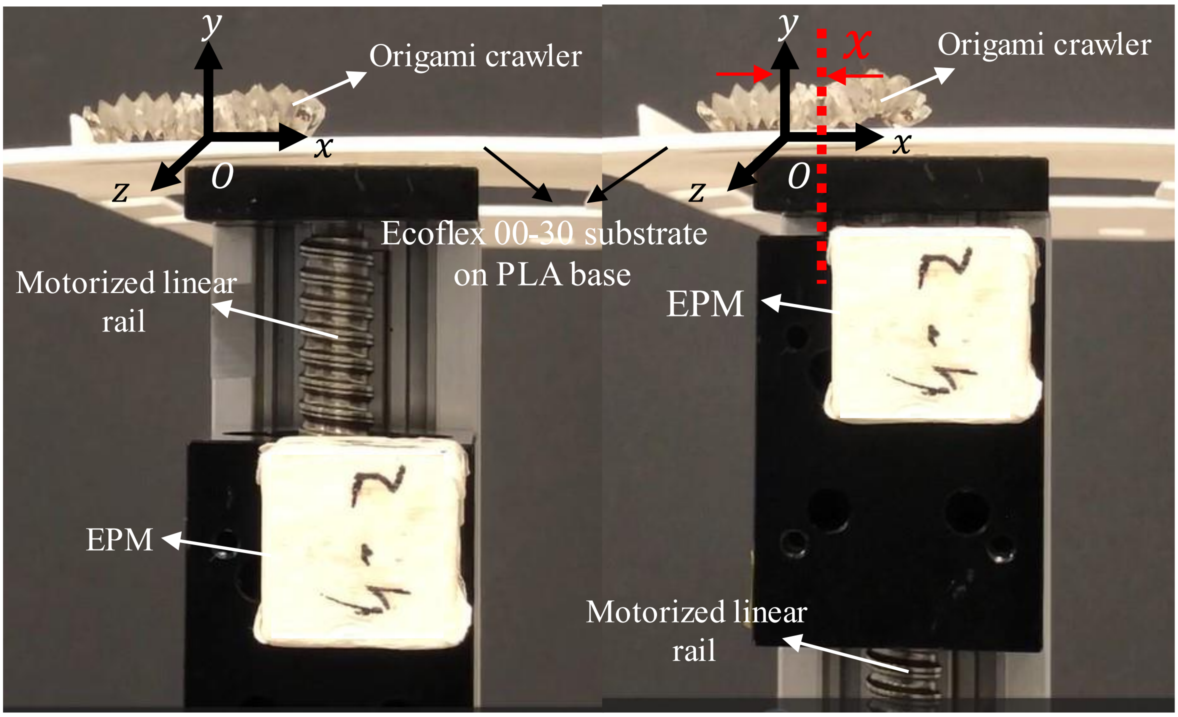

Fig. S 10 Experimental set for inducing directional locomotion of origami crawler. A motorized linear rail was used to vary the $\boldsymbol{y}$-position of the north pole of the EPM relative to the origami crawler. The $\boldsymbol{z}$-position of the EPM relative to the origami crawler was fixed at zero, while the $\boldsymbol{x}$-position of the EPM relative to the origami crawler was fixed at a fix distance away from the origin. The $\boldsymbol{x}$-position of the central segment of the origami crawler was tracked as a representation of the displacement of the crawler.

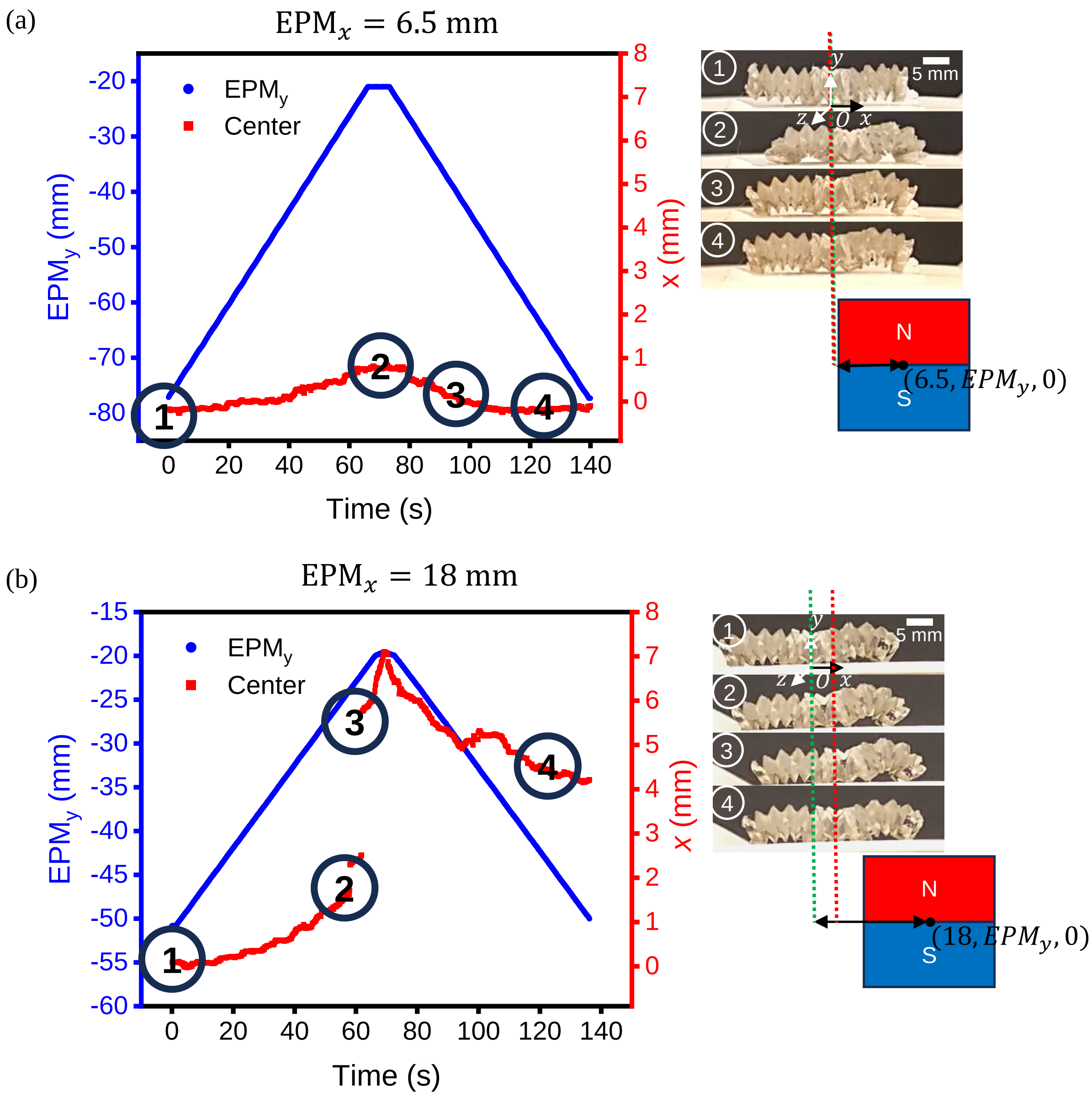

Fig. S 11 Position of the EPM relative to the front end of the origami crawler affects directional locomotion. (a) Placing the north pole of the EPM too close to the center of the origami spring resulted in little to no net displacement. (b) Placing the north pole of the EPM too far ahead from the center of the origami spring resulted in undesirable slippage.

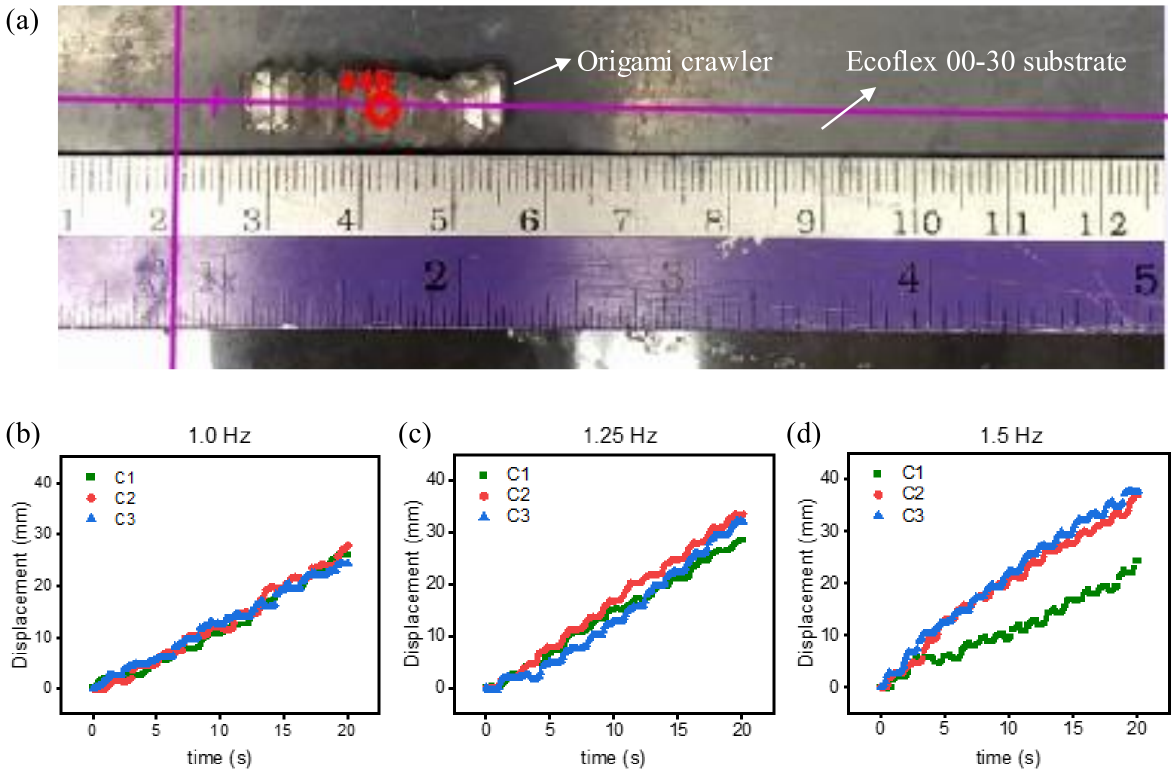

Fig. S 12 Speed of the Origami crawler. (a) The origami crawler was manually actuated on Ecoflex 00-10 at different frequencies. The position of the center of the crawler over time using the Physlets tracker, which was used to reflect the distance the crawler travelled for actuation frequencies of (b) 1.0 Hz, (c) 1.25 Hz, and (c) 1.5 Hz.

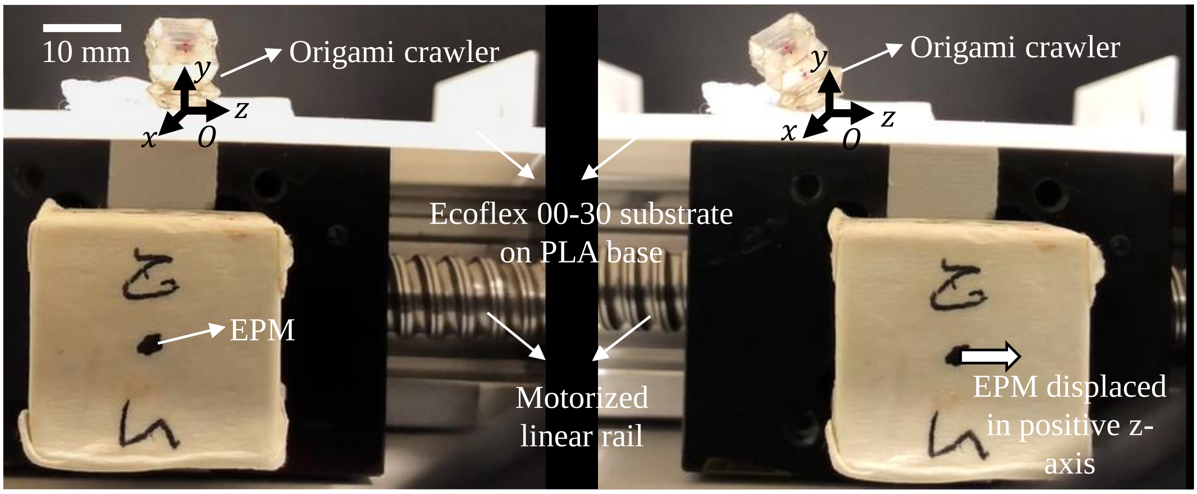

Fig. S 13 Experimental setup for the tilting of origami crawler. A motorized linear rail was used to vary the z-position of the north pole of the EPM relative to the origami crawler. The x-position of the EPM relative to the origami crawler was fixed at zero, while the y-position of the EPM relative to the origami crawler was fixed at a fix distance away from the origin (25 mm). The tilting angle of the central segment of the origami crawler was tracked.

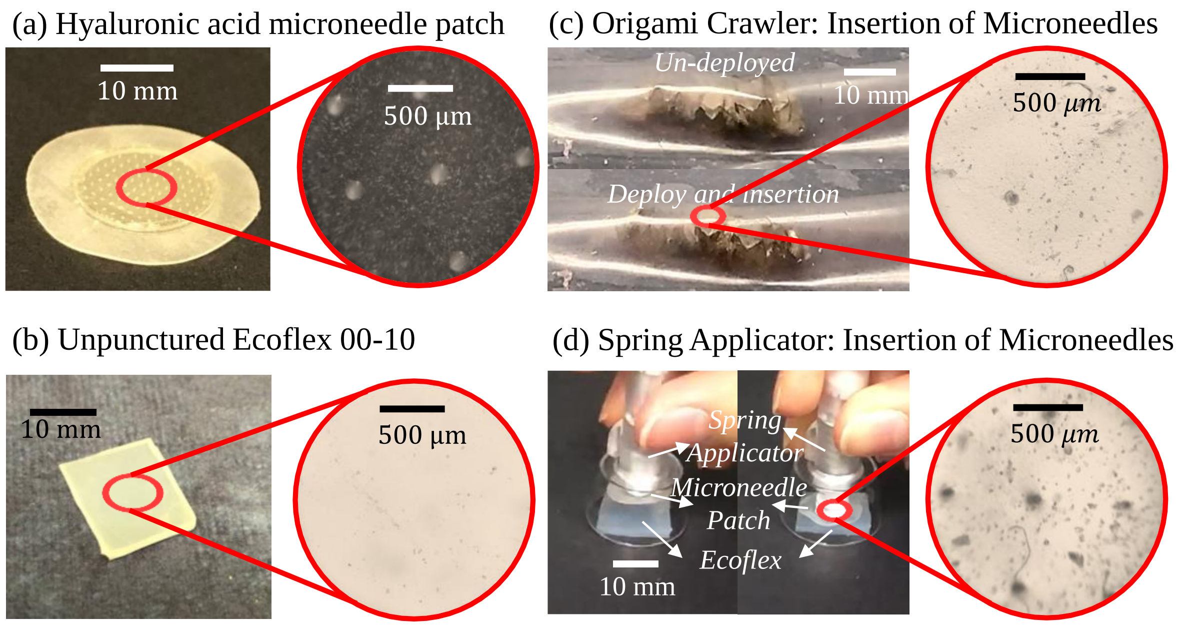

Fig. S 14 Optical microscope images for the verification of the insertion of microneedles into an Ecoflex film. (a) Topology of the CASMA microneedles patch used. (b) Topology of an un-punctured Ecoflex film. (c) Ecoflex film punctured by microneedles inserted by the origami spring. (d) Ecoflex film punctured by microneedles inserted by a commercial spring-loaded applicator.

Supplementary Tables

Table. S 1 Magnetic field strength required to deploy the bistable V-fold mechanism

Sample	Cycle	EPM_y Deployment (mm)	STDEV	B-field deployment (mT)	STDEV
S1	D1	26.46129838	[redacted]	87.76446797	[redacted]
	D2	28.72971286		70.79670255	
	D3	28.13795256		74.85900823	
S2	D1	26.36267166		88.59311098	
	D2	26.46129838		87.76446797	
	D3	27.15168539		82.18726069	
S3	D1	28.53245943		72.12418385	
	D2	26.75717853		85.32701523	
	D3	26.06679151		91.12864487	
Average		27.18456097	1.016621	82.28276248	7.727252

Table. S 2 Magnetic field strength required to undeploy the bistable V-fold mechanism

Sample	Cycle	EPM_y Undeployment (mm)	STDEV	B-field Undeployment (mT)	STDEV
	UD1	16.89450687	[redacted]	134.226077	[redacted]
	UD2	19.06429463		108.6612525	
S1	UD3	18.8670412		110.7629612	
	UD1	17.0917603		131.666085	
	UD2	16.59862672		138.1620031	
S2	UD3	16.89450687		134.226077	
	UD1	20.14918851		97.81450152	
	UD2	22.71348315		76.40455957	
S3	UD3	20.83957553		91.50015269	
Average		18.79033153	2.13293	113.7137411	22.1753

Table. S 3 Travelling speed of the origami crawler at different actuation frequencies

Actuation freq	Cycle	Speed (mm/s)	Bodylength/s	Average Speed (mm/s)	Speed STDEV	Average Bodylength/s	Bodylength/s STDEV
1.0 Hz	C1	1.28176	0.058262	1.28757	0.0958	0.058526	0.004357
	C2	1.38618	0.063008				
	C3	1.19476	0.054307				
1.25 Hz	C1	1.41346	0.064248	1.5566	0.1291	0.070755	0.005869
	C2	1.66426	0.075648				
	C3	1.59214	0.07237				
1.5 Hz	C2	1.84004	0.083638	1.85657	0.0234	0.084389	0.001062
	C3	1.87310	0.085141				

Table. S 4 Comparison of travelling speed of bistable origami crawler against literature

Actuation principle	Locomotion achieved	Normalized velocity to 3 s.f. (body length/s)	Ref
Magnetic	In-plane	0.0294	[19]
Light	In-plane	0.0345	[20]
Motor	In-plane	0.0204	[21]
Motors	In-plane	0.106	[22]
SMA	In-plane	0.00308	[23]
Magnetic	Out-of-plane	0.0418	[24]
Magnetic	Out-of-plane	0.00833	[25]
Magnetic	Out-of-plane	2.31	[26]
Magnetic	Out-of-plane	2.87	[27]
SMA	Out-of-plane	0.0667	[28]
Magnetic	In-plane	0.66	[29]
thermal	Out-of-plane	0.012	[30]
Magnetic	Out-of-plane	0.084389	Our work

Legends for Supplementary Movies

Supplementary Movie 1. Deployment and Undeployment of Bistable V-fold

Supplementary Movie S2. Steering on porcine tissue

Supplementary Movie S3. Crawling in confined spaces

Supplementary Movie S4. Crawling in porcine small intestine

Supplementary Movie S5. Microneedle delivery and insertion

SI References

[1] P. Jackson, *Folding Techniques for Designers-From Sheet to Form*. Laurence King Publishing, 2011.

[2] S. Miyashita, C. D. Onal, and D. Rus, “Self-pop-up cylindrical structure by global heating,” in *2013 IEEE/RSJ International Conference on Intelligent Robots and Systems*, IEEE, 2013, pp. 4065–4071.

[3] A. Ghassaei, E. D. Demaine, and N. Gershenfeld, “Fast, interactive origami simulation using GPU computation,” *Origami*, vol. 7, pp. 1151–1166, 2018.

[4] A. Reid, F. Lechenault, S. Rica, and M. Adda-Bedia, “Geometry and design of origami bellows with tunable response,” *Phys Rev E*, vol. 95, no. 1, p. 13002, 2017.

[5] R. Connelly, I. Sabitov, and A. Walz, “The bellows conjecture,” *Beitr. Algebra Geom*, vol. 38, no. 1, pp. 1–10, 1997.

[6] J. Butler *et al.*, “Highly compressible origami bellows for harsh environments,” in *International Design Engineering Technical Conferences and Computers and Information in Engineering Conference*, American Society of Mechanical Engineers, 2016, p. V05BT07A001.

[7] J. L. Silverberg *et al.*, “Origami structures with a critical transition to bistability arising from hidden degrees of freedom,” *Nat Mater*, vol. 14, no. 4, pp. 389–393, 2015, doi: 10.1038/nmat4232.

[8] D. Melancon, A. E. Forte, L. M. Kamp, B. Gorissen, and K. Bertoldi, “Inflatable origami: Multimodal deformation via multistability,” *Adv Funct Mater*, vol. 32, no. 35, p. 2201891, 2022.

[9] V. K. Venkiteswaran, D. K. Tan, and S. Misra, “Tandem actuation of legged locomotion and grasping manipulation in soft robots using magnetic fields,” *Extreme Mech Lett*, vol. 41, p. 101023, 2020.

[10] J. J. Abbott, E. Diller, and A. J. Petruska, “Magnetic Methods in Robotics,” *Annu Rev Control Robot Auton Syst*, vol. 3, no. 1, pp. 57–90, May 2020, doi: 10.1146/annurev-control-081219-082713.

[11] D. Brown and A. J. Cox, “Innovative uses of video analysis,” *Phys Teach*, vol. 47, no. 3, pp. 145–150, 2009.

[12] S. Miyashita, S. Guitron, K. Yoshida, S. Li, D. D. Damian, and D. Rus, “Ingestible, controllable, and degradable origami robot for patching stomach wounds,” *Proc IEEE Int Conf Robot Autom*, vol. 2016-June, no. 5, pp. 909–916, 2016, doi: 10.1109/ICRA.2016.7487222.

[13] J. L. Sparks *et al.*, “Use of silicone materials to simulate tissue biomechanics as related to deep tissue injury,” *Adv Skin Wound Care*, vol. 28, no. 2, pp. 59–68, 2015.

[14] M. Engers, K. W. Stewart, J. Liu, and P. P. Pott, “Development of a realistic venepuncture phantom,” *Current Directions in Biomedical Engineering*, vol. 6, no. 3, pp. 402–405, 2020.

[15] S. Miyashita, S. Guitron, K. Yoshida, S. Li, D. D. Damian, and D. Rus, “Ingestible, controllable, and degradable origami robot for patching stomach wounds,” *Proceedings - IEEE International Conference on Robotics and Automation*, vol. 2016-June, no. 5, pp. 909–916, 2016, doi: 10.1109/ICRA.2016.7487222.

[16] J. L. Sparks *et al.*, “Use of silicone materials to simulate tissue biomechanics as related to deep tissue injury,” *Advances in skin & wound care*, vol. 28, no. 2, pp. 59–68, 2015.

[17] M. Engers, K. W. Stewart, J. Liu, and P. P. Pott, “Development of a realistic venepuncture phantom,” *Current Directions in Biomedical Engineering*, vol. 6, no. 3, pp. 402–405, 2020.

[18] G. Traverso *et al.*, “Microneedles for drug delivery via the gastrointestinal tract,” *J Pharm Sci*, vol. 104, no. 2, pp. 362–367, 2015, doi: 10.1002/jps.24182.

[19] H. Lu *et al.*, “A bioinspired multilegged soft millirobot that functions in both dry and wet conditions,” *Nature Communications*, vol. 9, no. 1, 2018, doi: 10.1038/s41467-018-06491-9.

[20] M. Rogóż, H. Zeng, C. Xuan, D. S. Wiersma, and P. Wasylczyk, “Light-Driven Soft Robot Mimics Caterpillar Locomotion in Natural Scale,” *Advanced Optical Materials*, vol. 4, no. 11, pp. 1689–1694, 2016, doi: 10.1002/adom.201600503.

[21] H. Fang, Y. Zhang, and K. W. Wang, “Origami-based earthworm-like locomotion robots,” *Bioinspiration and Biomimetics*, vol. 12, no. 6, p. 65003, 2017, doi: 10.1088/1748-3190/aa8448.

[22] E. Vander Hoff, D. Jeong, and K. Lee, “OrigamiBot-I: A thread-actuated origami robot for manipulation and locomotion,” *IEEE International Conference on Intelligent Robots and Systems*, no. Iros, pp. 1421–1426, 2014, doi: 10.1109/IROS.2014.6942743.

[23] C. D. Onal, R. J. Wood, and D. Rus, “An origami-inspired approach to worm robots,” *IEEE/ASME Transactions on Mechatronics*, vol. 18, no. 2, pp. 430–438, 2013, doi: 10.1109/TMECH.2012.2210239.

[24] E. B. Joyee and Y. Pan, “A Fully Three-dimensional printed inchworm-inspired soft robot with magnetic actuation,” *Soft robotics*, vol. 6, no. 3, pp. 333–345, 2019, doi: 10.1089/soro.2018.0082.

[25] V. K. Venkiteswaran, L. F. P. Samaniego, J. Sikorski, and S. Misra, “Bio-inspired terrestrial motion of magnetic soft millirobots,” *IEEE Robotics and Automation Letters*, vol. 4, no. 2, pp. 1753–1759, 2019, doi: 10.1109/LRA.2019.2898040.

[26] S. H. Kim, S. Hashi, and K. Ishiyama, “Hybrid magnetic mechanism for active locomotion based on inchworm motion,” *Smart materials and structures*, vol. 22, no. 2, p. 27001, 2012.

[27] K. Lee, Y. Kim, J. K. Paik, and B. Shin, “Clawed miniature inchworm robot driven by electromagnetic oscillatory actuator,” *Journal of Bionic Engineering*, vol. 12, no. 4, pp. 519–526, 2015.

[28] J. S. Koh and K. J. Cho, “Omegabot: Biomimetic inchworm robot using SMA coil actuator and smart composite microstructures (SCM),” *2009 IEEE International Conference on Robotics and Biomimetics, ROBIO 2009*, pp. 1154–1159, 2009, doi: 10.1109/ROBIO.2009.5420752.

[29] Z. Qiji *et al.*, “Soft robotic origami crawler,” *Science Advances*, vol. 8, no. 13, p. eabm7834, Apr. 2022, doi: 10.1126/sciadv.abm7834.

[30] S. Wu, Y. Hong, Y. Zhao, J. Yin, and Y. Zhu, “Caterpillar-inspired soft crawling robot with distributed programmable thermal actuation,” *Science advances*, vol. 9, no. 12, p. eadf8014, 2023, doi: 10.1126/sciadv.adf8014.

1